

# Organic Electrochemical Transistors functionalized with Protein Minibinders for Sensitive and Specific Detection of SARS-CoV-2

Po-Chun Huang, Ying Zhou, Erin B. Porter, Ravindra G. Saxena, Andrea Gomez, Matthew Ykema, Naomi L. Senehi, Dongjoo Lee, Chia-Ping Tseng, Pedro J. Alvarez, Yizhi J. Tao, Yilin Li, and Rafael Verduzco\*

There is a need for rapid, sensitive, specific, and low-cost virus sensors. Recent work has demonstrated that organic electrochemical transistors (OECTs) can detect the severe acute respiratory syndrome coronavirus 2 (SARS-CoV-2) spike protein. Here, a simple and low-cost approach to the fabrication of OECT devices with excellent stability and unprecedented sensitivity and specificity for the detection of SARS-CoV-2 virus is demonstrated. The devices rely on the engineered protein minibinder LCBI, which binds strongly to SARS-CoV-2. The resulting devices exhibit excellent sensitivity for the detection of SARS-CoV-2 virus and SARS-CoV-2 spike protein receptor binding domain (RBD). These results demonstrate a simple, effective, and low-cost biomolecular sensor applicable to the real-time detection of SARS-CoV-2 virus and a general strategy for OECT device design that can be applied for the detection of other pathogenic viruses.

## 1. Introduction

Despite unprecedented efforts to contain the disease and mitigate its effects, the coronavirus disease 2019 (COVID-19) continues to impact our daily lives. As of January 2023, there were over 750 million confirmed cases of COVID-19 and over 6.8 million deaths globally attributed to this disease.<sup>[1]</sup> Though the global vaccination rate is over 50 percent, variants of the severe acute respiratory syndrome coronavirus 2 (SARS-CoV-2), the virus that causes COVID-19, continues to significantly disrupt the economy and healthcare facilities worldwide. COVID-19 can be highly contagious even before the appearance of symptoms, and SARS-CoV-2 can spread between people through droplet, airborne,

and fomite transmission.<sup>[2–6]</sup> While low-cost point-of-care (POC) tests are now widely available and many communities have returned to normal activities, approaches to quickly detect SARS-CoV-2 are still needed to mitigate exposure and protect the most vulnerable. Additionally, tests developed for the detection of SARS-CoV-2 can potentially be adapted for the monitoring and detection of other pathogenic viruses, such as flu viruses, noroviruses, or novel pathogenic viruses that may arise in the future.

Nucleic acid amplification tests such as reverse transcription polymerase chain reaction (RT-PCR) offer sensitive and accurate detection of COVID-19 and are currently the gold standard for testing for COVID-19.<sup>[7–9]</sup> However, RT-PCR requires specialized instrumentation and well-trained operators, and as a result testing by RT-PCR can be cumbersome and time consuming, making it unsuitable for continuous monitoring.<sup>[10]</sup> An alternative for point-of-care testing is the detection of SARS-CoV-2 antigens and antibodies. Lateral flow immunoassay tests for antigen and antibody are fast, low-cost, user friendly, and easy to find in pharmacies.<sup>[11–13]</sup> However, these tests have much poorer sensitivities and they are only recommended for use after symptoms have appeared.<sup>[14,15]</sup>

Recent work has focused on alternative sensors to SARS-CoV-2 that are rapid, sensitive, and can detect SARS-CoV-2 even in the presence of competing viruses. Examples include

P.-C. Huang, E. B. Porter, A. Gomez, D. Lee, C.-P. Tseng, Y. Li, R. Verduzco  
Department of Chemical and Biomolecular Engineering  
Rice University

Houston, TX 77005, USA  
E-mail: rafaelv@rice.edu

Y. Zhou, M. Ykema, Y. J. Tao  
Department of BioSciences  
Rice University


Houston, TX 77005, USA

R. G. Saxena  
Applied Physics Program  
Rice University

Houston, TX 77005, USA

N. L. Senehi, P. J. Alvarez  
Department of Civil and Environmental Engineering  
Rice University

6100 Main Street, Houston, TX 77005, USA

 The ORCID identification number(s) for the author(s) of this article can be found under <https://doi.org/10.1002/admi.202202409>

© 2023 The Authors. Advanced Materials Interfaces published by Wiley-VCH GmbH. This is an open access article under the terms of the Creative Commons Attribution License, which permits use, distribution and reproduction in any medium, provided the original work is properly cited.

DOI: 10.1002/admi.202202409

plasmonic biosensors,<sup>[16,17]</sup> electrochemical biosensors,<sup>[18,19]</sup> field-effect transistors,<sup>[20,21]</sup> and organic electrochemical transistors (OECTs).<sup>[22]</sup> Organic electrochemical transistors (OECTs) are of particular interest because they can be fabricated inexpensively and have excellent sensitivity for biomolecular detection due to their high transconductance.<sup>[23]</sup> Guo et al. developed OECT sensors for rapid single-molecule detection of SARS-CoV-2.<sup>[22]</sup> They introduced nanobodies that were designed from the antigen-binding domain (VHH) of SARS-CoV-2 antibodies to functionalize the gate electrodes. Their devices provided a fast response (< 15 min from sample to result) and excellent sensitivity with a limit-of-detection (LOD) of  $1.2 \times 10^{-21}$  M for the SARS-CoV-2 S1 spike proteins in human saliva, where the LOD was defined as the lowest concentration where the devices produced a normalized response that was equal to the noise level plus three times the noise standard deviation.<sup>[24]</sup> Liu et al. also developed portable OECT biosensors for the SARS-CoV-2 antibody detection.<sup>[25]</sup> By immobilizing the SARS-CoV-2 spike proteins on the gate electrode of an OECT, they were able to detect antibodies for SARS-CoV-2 to concentrations down to  $1 \times 10^{-15}$  M (1 fM) in aqueous solutions and  $1 \times 10^{-14}$  M (10 fM) in serum and saliva within 5 min. Despite these significant achievements, these studies focused primarily on detection of the SARS-CoV-2 spike protein or SARS-CoV-2 antibodies rather than direct detection of the SARS-CoV-2 virus. Additionally, these studies relied on photolithography techniques for device fabrication, which are costly and may be impractical for widely-used POC devices. Finally, these prior tests did not comprehensively investigate the time-dependence of the sensor response.

In this work, we report a novel design and fabrication approach to making OECTs that can directly detect SARS-CoV-2 at concentrations as low as 40 virus particles per mL (TCID<sub>50</sub>/mL), even in the presence of other viruses. We comprehensively investigated the response of the sensors to both the SARS-CoV-2 spike protein and virus, including understanding the time-dependent response of the sensors and testing for interference from other proteins and viruses. Our fabrication approach does not require photolithography, and we implemented a simple two-step approach to functionalize the OECT device for binding to SARS-CoV-2 spike protein and virus. Importantly, we took advantage of a novel protein minibinder for the specific detection of SARS-CoV-2. Protein minibinders are small engineered proteins with greater stability and lower cost than enzymes or antibodies.<sup>[26]</sup> The resulting devices could be quickly fabricated and were effective for detecting the presence of SARS-CoV-2 spike protein receptor binding domain (SARS-CoV-2 RBD) and the inactive SARS-CoV-2 within 10 and 15 min and determining the concentration of protein or virus present within 30 min. Overall, we demonstrate a simple, effective, and low-cost biomolecular sensor to detect SARS-CoV-2 and a general strategy for OECT device fabrication that can be applied to the detection of other pathogenic viruses.

## 2. Results and Discussion

Our goal was to develop a rapid, low-cost method for the fabrication of OECT sensors with excellent sensitivity and specificity for the detection of SARS-CoV-2 and to comprehensively investigate the device sensitivity, response time, and stability. The OECT

sensors contained gold source and drain electrodes, an Ag/AgCl gate electrode, and PEDOT:PSS channel. The PEDOT:PSS channel was functionalized with the engineered protein minibinder LCB1 immobilized on the PEDOT:PSS channel of an OECT device (Figure 1). LCB1 is a 56-aa protein minibinder designed to bind strongly to the SARS-CoV-2 spike protein receptor binding domain (SARS-CoV-2 RBD). LCB1 blocks the ACE2 receptor and inhibits SARS-CoV-2 infection in cell culture. LCB1 is also much smaller than antibodies ( $\approx 5\%$  of the size of a full antibody) and exhibits excellent stability at elevated temperatures.<sup>[27]</sup> Protein minibinders like LCB1 are therefore attractive for the development of low-cost and stable biosensors, and the present study is the first example of a protein minibinder integrated with an OECT. We expressed recombinant LCB1 in *E. coli* with a cleavable 6xHis tag at the N-terminus to facilitate protein purification and a 10xGS linker with a single cysteine at the C-terminus.

Prior to evaluating the devices, we quantified the binding affinity of LCB1 to the SARS-CoV-2 RBD using bio-layer interferometry (BLI). The results of these measurements for concentrations of 2.5, 5, and 10 nM LCB1 are provided in the Figure S1 (Supporting Information). The dissociation constant  $K_D$  for binding between LCB1 and SARS-CoV-2 RBD was 3.95 nM, and the association and dissociation rate constants were  $1.88 \times 10^6 \text{ M}^{-1} \text{ s}^{-1}$  and  $7.42 \times 10^{-3} \text{ s}^{-1}$ , respectively. These measurements reflect strong binding affinity between LCB1 and the SARS-CoV-2 RBD. As a point of comparison, a prior study reported that the  $K_D$  values of SARS-CoV-2 and the angiotensin converting enzyme-2 (ACE2) was 4.7 nM.<sup>[28]</sup>

We also performed native polyacrylamide gel electrophoresis (native PAGE) to test the binding between LCB1 and SARS-CoV-2 RBD in solution (Figure S2a, Supporting Information). Native PAGE was performed on SARS-CoV-2 RBD alone, LCB1 alone, and the mixture of LCB1 and SARS-CoV-2 RBD. LCB1 and SARS-CoV-2 RBD gave distinct migration behaviors while LCB1 gave rise to a single band and RBD did not migrate, presumably due to its net positive charge. When SARS-CoV-2 RBD was mixed with LCB1 in solution, the LCB1 band disappeared, indicating that LCB1 was bound to SARS-CoV-2 spike protein RBD. We also evaluated the stability of LCB1 when stored at either 25 or 4 °C by running sodium dodecyl sulfate polyacrylamide gel electrophoresis (SDS-PAGE) tests for LCB1 stored for up to 9 days (Figure S2b,c, Supporting Information). No degradation was observed when the protein was stored at either 25 or 4 °C. A similar experiment performed for up to 7 weeks at 25 °C revealed no degradation of LCB1, indicating that the protein can remain stable when stored in electrolyte at room temperature (Figure S2d, Supporting Information).

Next, we immobilized LCB1 onto the PEDOT:PSS channel of our OECT devices. Our approach to modifying the PEDOT:PSS channel involved using polyvinyl alcohol (PVA) as an additive and crosslinker to introduce hydroxyl functionalities on the channel surface (see Experimental Section for additional details). The channel was modified with an organosilane epoxy GOPS through vapor deposition, which introduces epoxy functionalities on the device surface. LCB1 was then immobilized onto the channel by adding a solution of LCB1 directly to the electrolyte well. The terminal amine or cysteine of LCB1 can react with the epoxy group to covalently tether the LCB1 to the channel surface (Figure 2a). We verified the immobilization of LCB1 using

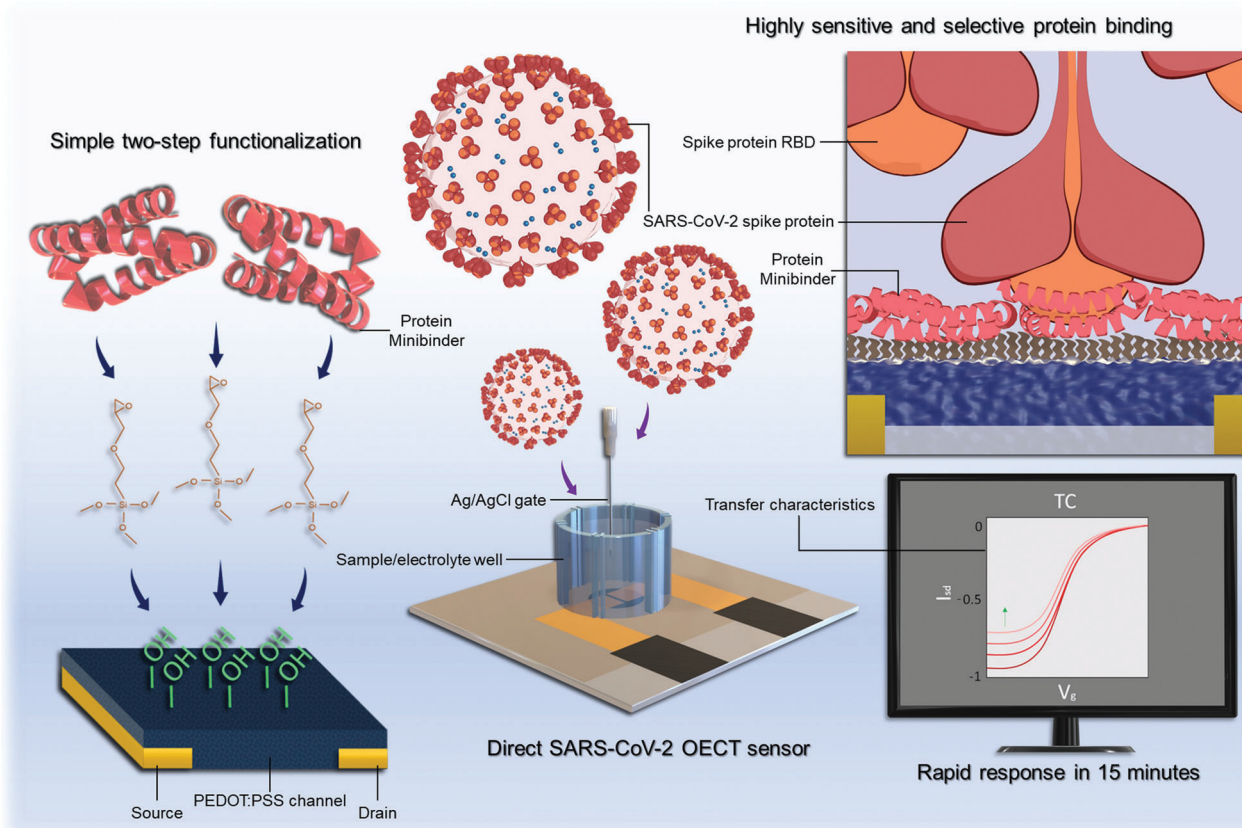


**Figure 1.** Design and fabrication of OECTs for the detection of SARS-CoV-2. The OECT includes gold source-drain electrodes, a PEDOT:PSS channel, and an Ag/AgCl gate electrode. Protein minibinders that bind to SARS-CoV-2 are immobilized on the surface of the PEDOT:PSS channel, and binding of the SARS-CoV-2 spike protein RBD or virus can be detected by monitoring changes in the source-drain current.

X-ray photoelectron spectroscopy (XPS) measurements, which revealed the emergence of Si2p peaks ( $\approx 100$  eV) after modification of the channel with GOPS and an N1s peak ( $\approx 400$  eV) after grafting of LCB1 (Figure 2b). We also performed QCM-D measurements to quantify the mass of LCB1 adsorbed onto the surface. These measurements were performed by preparing two films of PEDOT:PSS on a silicon dioxide sensor and modifying one with GOPS (Figure 2c). The sensors were stabilized in PBS buffer prior to introducing LCB1, and in both cases the resonant frequency decreased, which reflects binding of the LCB1 to the sensor. However, the sensor without GOPS had only a small change in frequency ( $\Delta f$ ) of 22.33 Hz compared with a much larger change of 215.25 Hz for the GOPS-modified sensor. The unmodified sensor also showed reversible binding of the LCB1, where the change in frequency decreased and then increased and stabilized at a value of  $\approx 22$  Hz. A comparison of these two sensors shows stronger and more stable binding to the GOPS modified electrode, likely due to reaction between the LCB1 and GOPS. Additionally, the change in frequency corresponds to a change in sensor mass of  $1270 \text{ ng cm}^{-2}$ . Using the calculated molecular weight of 8.6 kDa for LCB1 and an estimated cross-sectional diameter of 0.5 nm for the LCB1 protein,<sup>[27]</sup> this corresponds to  $\approx 17.4\%$  surface coverage.

Electrochemical measurements provide additional evidence that the LCB1 bound covalently to the PEDOT:PSS channel

(Figure 2d). The capacitance of the PEDOT:PSS channel was much higher than that of bare gold electrodes, as expected. After binding of the LCB1 to the channel, a reduction in capacitance was observed. This is expected because the LCB1 bound to the channel surface introduces an additional interfacial resistance and reduces the potential at the electrolyte-electrode interface. We also performed electrochemical impedance spectroscopy (EIS) measurements to quantify changes in the impedances of the devices. Specifically, we measured devices with unmodified PEDOT:PSS, PEDOT:PSS with LCB1, and PEDOT:PSS and LCB1 after exposure to  $47 \mu\text{M}$  SARS-CoV-2 protein receptor binding domain (RBD) (Figure S4, Supporting Information). These measurements revealed a clear increase in impedance across this series of devices and enabled us to extract the charge transfer resistance for each device. The charge transfer resistance increased from 121.6 to 130.8  $\Omega$  after LCB1 immobilization, and the charge transfer resistance further increased to 134.4  $\Omega$  after exposure to a high concentration ( $47 \mu\text{M}$ ) SARS-CoV-2 RBD.

After confirming the binding of LCB1 protein to PEDOT:PSS, we focused on fabrication and testing of OECT devices functionalized with LCB1. The OECT devices were made without relying on cleanroom techniques. Kapton tape was used as a mask to define the source and drain electrodes and PEDOT:PSS was spin cast from solution to create the channel (see Figure S3, Supporting Information). This approach enabled rapid device fabrication

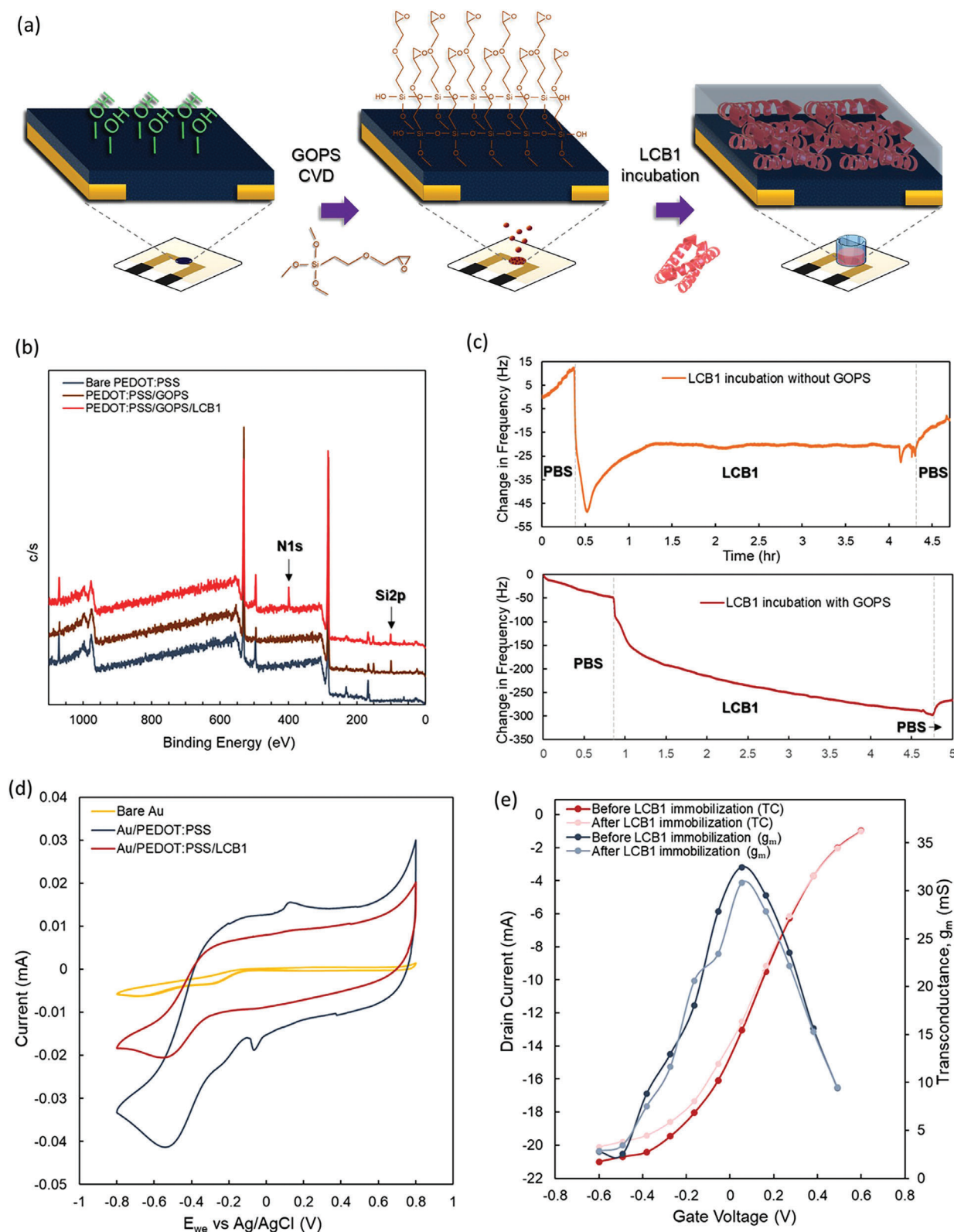


**Figure 2.** Design and characterization of LCB1 functionalized channel. a) Channel functionalization involving vapor deposition of GOPS followed by covalent attachment of LCB1 protein minibinder. b) XPS analysis of bare PEDOT:PSS thin films, films after deposition of GOPS, and films after LCB1 immobilization. c) QCM-D data of the LCB1 incubation with and without GOPS functionalization. d) CV analysis of bare gold, PEDOT:PSS/gold, and LCB1/PEDOT:PSS/gold. e) Transfer characteristics and transconductances of the OECTs before and after LCB1 immobilization. The measurement was performed with  $V_g = -0.6$  to  $0.6$  V, a delay time of  $0.5$  s, and  $0.1$  V steps. The drain voltage was  $-0.6$  V.

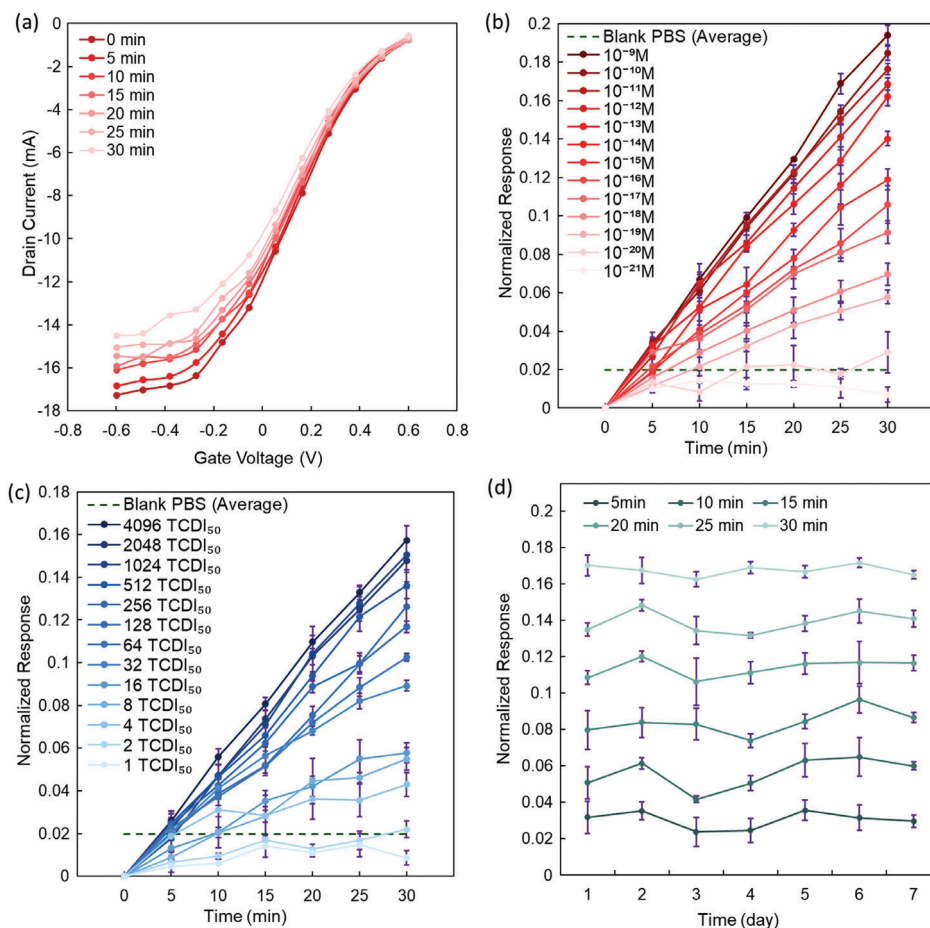


**Figure 3.** Performance of LCB1-functionalized OECTs for detection of SARS-CoV-2 RBD and virus. a) Transfer characteristics of LCB1-functionalized OECT as a function of incubation time after adding  $10^{-12}$  M SARS-CoV-2 RBD. The drain current decreases with incubation time, reflecting increasing amounts of SARS-CoV-2 binding to the channel. b) Normalized response (NR) of LCB1-functionalized OECT to SARS-CoV-2 RBD measured at  $V_g = -0.6$ , with concentration ranging from  $10^{-9}$  M to  $10^{-21}$  M. The NR increases with both SARS-CoV-2 RBD concentration and incubation time. c) NR of LCB1-functionalized OECT after addition of SARS-CoV-2 virus, with concentration ranging from 1 to 4096 TCID<sub>50</sub> per 250  $\mu$ l. d) NR of LCB1-functionalized OECT in response to  $10^{-12}$  M SARS-CoV-2 RBD for 30 min incubation time as a function of days since device fabrication. Normalized response values represent averages over at least three independent measurements. Error bars represent standard deviations.

and testing, and a representative transfer curves for our OECTs is shown in (Figure 2e). The amplitude of the source-drain current decreased from  $\approx 22$  mA to near 0 with increasing gate voltage. The transconductance, which reflects the slope of the drain current as a function of gate voltage, peaked at 32.5 mS at a gate voltage of 0.1 V. This value compares favorably with prior reports of PEDOT:PSS OECTs.<sup>[29]</sup> A slight reduction in the amplitude of the drain current and transconductance was observed after binding LCB1. This likely reflects the added resistance of the LCB1 and provides further direct evidence for modification of the channel by LCB1. These results demonstrate that our low-cost approach to OECT fabrication produces functional and effective OECT devices. However, a drawback of this approach is that it leads to significant device-to-device variations in the channel length and width, which directly impact the source-drain current. To account for these variations, the response current was normalized by the initial current (baseline) that measured in pure electrolyte for each device. This enables quantitative comparison across devices that differ in terms of channel dimensions, as demonstrated in the results that follow.

By monitoring the transfer characteristics of the LCB1-functionalized devices, we reproducibly detected both SARS-CoV-2 RBD and gamma-inactivated SARS-CoV-2 virus. Tests were performed by first collecting a baseline transfer curve in pure PBS buffer electrolyte, prior to introduction of SARS-CoV-2 RBD or SARS-CoV-2 virus. Next, a known concentration of SARS-CoV-2 RBD or SARS-CoV-2 virus was added to the well, and the device transfer characteristics were measured by scanning the gate voltage from -0.6 to 0.6 V. This measurement was repeated every five minutes for up to 30 min to provide a change in the transfer characteristics with time and, by repeating the measurement with different concentrations of protein or virus added, as a function of concentration. A representative test for  $10^{-12}$  M (1 pM) of SARS-CoV-2 RBD is shown in Figure 3a. The baseline transfer curve was measured prior to adding SARS-CoV-2 RBD to the electrolyte at 0 min. The conductance of the channel subsequently decreased continuously with time, as reflected in a reduction of the drain current amplitude over the entire range of gate voltages measured. After 30 min, the drop in the current amplitude at  $V_g = -0.6$  was 16%. This drop reflects binding of

the SARS-CoV-2 RBD to the channel, and the time dependence reflects diffusion limitations for the protein binding to the channel.

We achieved excellent consistency and reproducibility in testing by plotting the normalized response (NR) of the device at  $V_g = -0.6$  V in the transfer curves (Figure 3b–c). The NR is defined as the normalized change in the source drain current relative to the baseline,  $NR = (I - I_0)/I_0$  where  $I$  is the current measured every 5 min and  $I_0$  is the baseline current measured in pure PBS prior to adding the target biomolecule. The NR measurements were averaged over at least three independent devices for each condition tested. Despite device-to-device variations in channel dimensions, the NR was only dependent on the concentration of SARS-CoV-2 RBD concentration and incubation time. A higher concentration of SARS-CoV-2 RBD resulted in greater binding to the channel, which produced a greater change in device transfer characteristics. Similarly, longer incubation times enable greater binding of the protein to the channel, resulting in a larger NR. Up to 30 min incubation time, the NR increases linearly with incubation time. Additionally, at very low SARS-CoV-2 RBD concentrations,  $10^{-20}$  M and below, the NR is statistically indistinguishable from the baseline transfer curve.

To quantify the sensitivity of the devices, we calculated the limit of detection (LOD) for detection of SARS-CoV-2 RBD. Since the NR varies with SARS-CoV-2 RBD concentration and incubation time, the LOD depends on concentration and incubation time. Details on the calculation of the LOD are provided in the Supplementary Materials. Briefly, we first measured a baseline transfer curve in devices with only PBS buffer in the electrolyte well. This was measured for five separate devices, which provided an average baseline along with a standard deviation. The minimum threshold for detection was then set as the baseline plus three times the standard deviation.<sup>[24]</sup> Next, we added SARS-CoV-2 RBD to the electrolyte well and measured transfer curves at five minute intervals. This was repeated at different concentrations and for at least three separate devices, providing an average NR as a function of time and concentration (see Figure S5–7, Supporting Information). This process was repeated for SARS-CoV-2 and for other biomolecular targets. The NR of the devices for the detection of SARS-CoV-2 RBD is presented in Figure 3 along with the baseline NR, and the LOD is approximately the concentration for which the NR is greater than the signal for PBS buffer (for a fixed incubation time). For 10 and 30 min incubation times, the LOD of the OECT devices was  $2.79 \times 10^{-15}$  M (2.79 fM) and  $2.60 \times 10^{-20}$  M (26 zM), respectively (Table S1, Supporting Information). By comparison, the LOD was only  $2.6 \times 10^{-4}$  M at 5 min. The LOD reported here compares favorably with that reported previously by Guo et al. for nanobody-functionalized OECTs for the detection of SARS-CoV-2 RBD.<sup>[22]</sup> For devices with PEDOT:PSS as the channel, Guo et al. measured an LOD of as low as  $4.8 \times 10^{-14}$  M for the detection of SARS-CoV-2 RBD. Notably, they obtained a much lower LODs under different conditions and for detection of SARS-CoV-2 spike protein. For example, their LOD was  $1.2 \times 10^{-21}$  M for detection of SARS-CoV-2 spike protein in saliva using the conjugated polymer p(gOT2-g6T2) as the channel material. Our sensors also compare favorably against other transistor-based sensors for detection of SARS-CoV-2 virus, proteins, or antibodies (Table S2, Supporting Information).

The OECT devices also displayed excellent sensitivity for the detection of inactive SARS-CoV-2 (Figure 3c). The virus concentration was varied from between 1 and 4096 TCID<sub>50</sub> per 250  $\mu$ L. The response was averaged over at least three devices for each virus concentration tested, and the response was monitored as a function of time. The NR increased with both virus concentration and with incubation time. After 15- and 30-min incubation times, the LOD was 156 and 17 TCID<sub>50</sub>/mL. This LOD can also be compared LOD for detection of inactive SARS-CoV-2 to that for the SARS-CoV-2 RBD. We should expect a lower LOD for the virus due to lower diffusivity of the virus and inaccessibility of some spike proteins on the surface. Each SARS-CoV-2 particle contains  $\approx 48$  spike proteins on the surface.<sup>[30]</sup> Therefore, an LOD of 17 TCID<sub>50</sub>/mL for detection of the inactive virus corresponds to  $\approx 816$  SARS-CoV-2 RBD/mL or a concentration of  $1.3 \times 10^{-18}$  M. As expected, this is higher than the LOD of  $2.60 \times 10^{-20}$  M for detection of the SARS-CoV-2 RBD. Finally, the LCB1-functionalized OECT devices displayed excellent stability. To test this, we measured the response of the OECTs to  $10^{-12}$  M SARS-CoV-2 RBD and 15 min incubation time after storing at room temperature in PBS buffer for up to 1 week. The devices were stable and insensitive to the duration of storage (Figure 3d).

In addition to being highly sensitive for the detection of SARS-CoV-2 spike RBD and virus, the devices were capable of specific detection when interfering proteins and viruses were added. To perform tests for specificity, we compared the responses of devices exposed to i) an interfering protein or virus or ii) exposed to a blend of the interfering protein or virus with SARS-CoV-2 RBD or SARS-CoV-2 virus. For interfering proteins, we selected human serum albumin (HSA), MERS-CoV S1S2, and SARS-CoV-1 S1S2. HSA is a protein that would be present in clinical samples, and the other two proteins come from different coronaviruses. As shown in Figure 4a–b, the NR remained below 0.2 when introducing a non-target protein at  $10^{-9}$  M. On the other hand, a blend of SARS-CoV-2 RBD ( $10^{-12}$  M) with non-target protein ( $10^{-9}$  M) produced a large change in NR over time, similar to that measured for devices responding to only SARS-CoV-2 RBD. The excellent specificity of LCB1-functionalized OECTs for detection of SARS-CoV-2 RBD is attributed to the low binding affinity between LCB1 and the spike proteins of MERS-CoV and SARS-CoV-1 compared to that between LCB1 and the SARS-CoV-2 RBD (Figure S1b, Supporting Information).

The sensors were also successful at detecting inactive SARS-CoV-2 virus in the presence of other viruses (Figure 4c). We tested the responses of the devices to either the human coronavirus OC43 (HCoV-OC43) or the H3N2 influenza A virus (1024 TCID<sub>50</sub>/mL) and compared the response to a blend of one of these viruses with inactive SARS-CoV-2 (128 TCID<sub>50</sub>/mL). The devices only responded when SARS-CoV-2 virus was present. The results of specificity testing are summarized in Figure 4d, where the sensors respond only to target virus or protein and are non-responsive to interfering proteins and viruses in solution.

### 3. Conclusion

This work demonstrates a sensitive, specific, and easy-to-fabricate biosensor for SARS-CoV-2 and establishes several important advances in terms of sensor design. First, we show that sensitive and accurate sensors can be fabricated. This simplifies

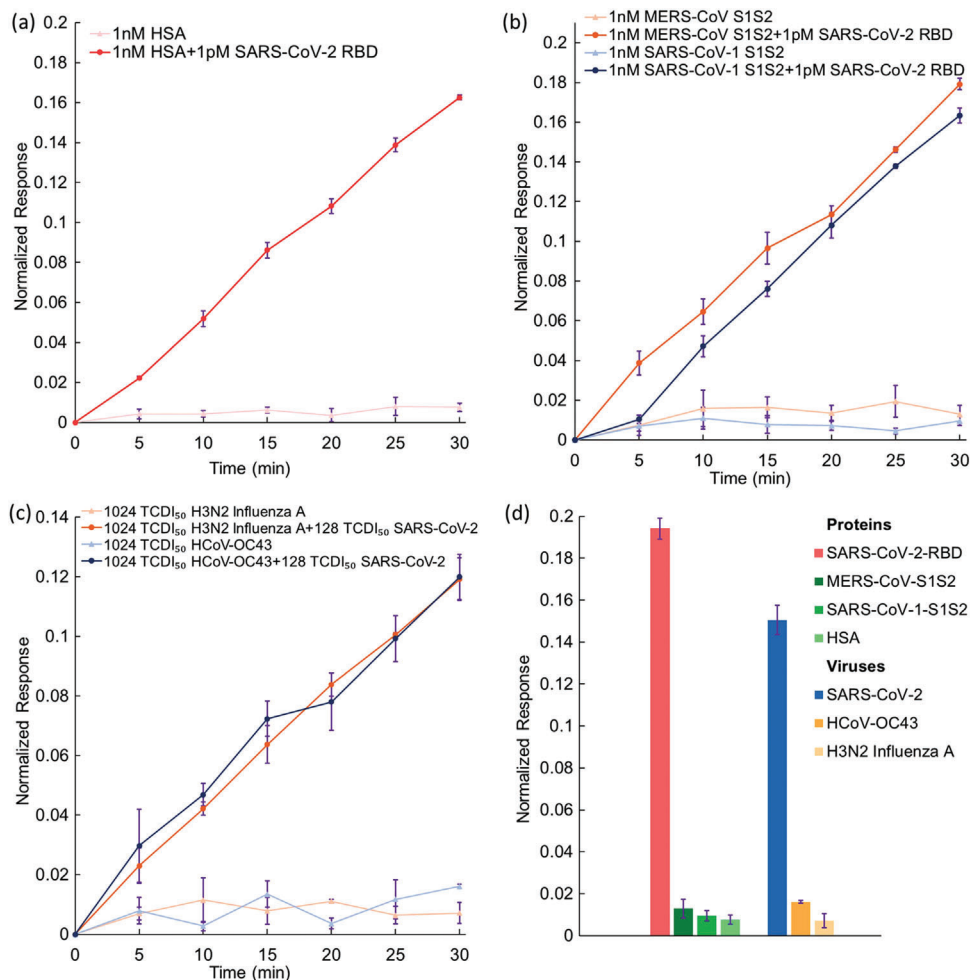


**Figure 4.** Specificity testing of LCB1-functionalized OECT. Specificity testing was performed by measuring the NR for LCB1-functionalized OECTs to SARS-CoV-2 RBD or virus in the presence of interfering proteins and viruses, respectively. a)  $10^{-9}$  (1 nM) Human serum albumin (HSA) and  $10^{-12}$  (1 pM) SARS-CoV-2 RBD. b)  $10^{-9}$  (1 nM) non-target coronavirus spike proteins MERS-CoV S1S2 and SARS-CoV-1 S1S2 and  $10^{-12}$  (1 pM) SARS-CoV-2 RBD. c) 1024 TCDI<sub>50</sub> non-target inactive viral particles H3N2 influenza A virus and HCoV-OC43 and 128 TCDI<sub>50</sub> SARS-CoV-2. d) Normalized response of OECTs to proteins and viruses tested, after 30 min incubation time and without blending proteins or viruses. Normalized response values represent averages over at least three independent measurements. Error bars represent standard deviations.

the device fabrication process and makes these sensors more accessible than previously reported OECTs. Although the raw current response exhibits significant device-to-device variability using our approach, we can directly and quantitatively compare the normalized response (NR) across multiple devices to generate a calibration curve and establish a limit-of-detection. These devices are therefore applicable for use as low-cost, portable sensors for SARS-CoV-2. On the other hand, a drawback of our approach is that each OECT must be normalized prior to its use as a sensor. Therefore, a sensing device would have to acquire a baseline for each new OECT used as a sensor.

Our work demonstrates that engineered protein minibinders like LCB1 are effective for detection. Protein minibinders like LCB1 are more robust than antibodies or enzymes, less expensive to produce, and can be as effective for binding to a specific biomolecular target. As our work demonstrates, protein minibinders can serve as the active transduction mechanism for electrochemical sensors like OECTs.

Future work should establish whether this approach to OECT fabrication can be extended for the detection of different viruses and proteins and whether the sensors can operate in different environments. All of our tests were performed in PBS buffer at room temperature under ambient conditions, and it is unclear whether the same sensors would be effective in different environments. For example, these devices could be of interest for monitoring SARS-CoV-2 in wastewater,<sup>[31,32]</sup> but would have to be insensitive to the presence of organic pollutants and contaminants. There may be interest in the development of similar devices for seawater monitoring, but would have to be robust in the presence of much higher salinities and lower temperatures. Additionally, since SARS-CoV-2 is transmitted in air, the OECT sensors demonstrated would ideally be paired with a technology for sampling air and trapping aerosols in a liquid condensed phase without destroying or damaging the virus.<sup>[33]</sup> Such a technology would enable passive monitoring of indoor spaces for the presence of aerosolized SARS-CoV-2 virus. Finally, this work has

potential relevance to the development of conformal and wearable chemical and bimolecular sensors.<sup>[34–36]</sup> Recent work has enabled stretchable and conformal OECTs that can be implemented for monitoring bioelectronic signals or detecting the presence of target biomarkers.<sup>[37–41]</sup> In combination with the work demonstrated here, this potentially enables wearable biomarker sensors with excellent sensitivity and specificity.

## 4. Experimental Section

**Reagents and Materials:** Poly(3,4-ethylenedioxythiophene) polystyrene sulfonate (Clevios™ PH1000) was purchased from Heraeus. Ethylene glycol (EG), (3-glycidyloxypropyl) trimethoxysilane (GOPS), 4-dodecylbenzenesulfonic acid (DBSA), pH 7.4 0.01 M phosphate buffered saline (PBS), poly(vinyl alcohol) (PVA), and human serum albumin (HSA) were purchased from Sigma Aldrich. The spike proteins of SARS-CoV-1 (SARS-CoV-1 S1S2), Middle East respiratory syndrome coronavirus (MERS-CoV S1S2) and SARS-CoV-2 receptor binding domain (SARS-CoV-2 RBD) were purchased from Sino Biological. Gamma-inactivated SARS-CoV-2 and human coronavirus OC43 (OC43) viral solutions were supplied by BEI Resources. Influenza A (H3N2) was provided by Dr. Robert Krug's lab at UT Austin. All chemicals, proteins and viral particles were used as received.

**Bio-Layer Interferometry:** ForteBio Octet Platform was used to perform bio-layer interferometry (BLI) to quantify the binding affinity of LCB1 to SARS-CoV-2 RBD. In the Octet assay, the binding between a ligand immobilized on the biosensor tip surface and an analyte in solution produces an increase in optical thickness at the biosensor tip, which results in a shift in the interference pattern measured in nanometers. The wavelength shift ( $\Delta\lambda$ ) is a direct measure of the change in optical thickness of the biological layer, which is directly proportional to the amount of analyte molecules bound at the biosensor tip. The baseline of the measurement was gained from running the buffer solution alone. Binding kinetics were monitored by dipping the biosensors in wells containing the target proteins at the indicated concentration (association step) and then dipping the sensors back into baseline/buffer (dissociation). When this shift is measured over a period, a classic association/dissociation curve was obtained. SARS-CoV-2 RBD was loaded onto biosensors at 20 nM in binding buffer (20 mM HEPES pH 7.5, 150 mM NaCl, 5 mM 2-Mercaptoethanol (2-ME)). LCB1 protein was diluted from concentrated stocks into binding buffer.

**SDS PAGE and Native PAGE:** Briefly, PAGE gels were made with a 4% stacking gel and a 15% separating gel. For sample preparation, protein samples were mixed at a 1:5 volume ratio with a 6x SDS sample loading buffer containing 375 mM Tris-HCl pH 6.8, 60% glycerol, 12% SDS, 600 mM DTT and 0.06% bromophenol blue. The mixture was boiled at 100 °C for 3 min and loaded into sample wells. Electrophoresis was performed at 100 V until the dye reached the bottom of the gel. Gels were first stained in buffer containing 0.1% Coomassie Brilliant Blue R250, 30% methanol and 10% acetic acid, and then de-stained in buffer containing 30% methanol and 10% acetic acid with gentle shaking. The native gels consisted of a 15% separating gel only. For native gel sample preparation, a 6x sample loading buffer was used that contained 600 mM Tris-HCl, 50% glycerol and 0.02% bromophenol blue.

**Preparation of Engineered LCB1 Protein Minibinder:** LCB1 is a 55aa protein designed to bind strongly to the SARS-COV-2 spike protein.<sup>[27]</sup> To facilitate protein purification and immobilization on the sensors, LCB1 cDNA was cloned into a pET-28a vector (GenScript) to express a recombinant LCB1 containing a N-terminal 6xHis-tag followed by a TEV cleavage site and a C-terminal 10xGS linker ending with a single cysteine residue. The plasmid was then transformed into Rosseta™ 2 (DE3) competent cells (Novagen, Cat.71400-3). For protein expression, *E. coli* cells at the phase of exponential growth were induced using 1 mM Isopropyl  $\beta$ -D-1-thiogalactopyranoside (IPTG) when OD<sub>600nm</sub> reached 0.6–0.8. After shaking overnight at 22 °C, cells were harvested by centrifugation at 4,000 g for 15 min and sonicated in lysis buffer containing 20 mM Tris pH8.0,

300 mM NaCl, 5% glycerol (v/v), 5 mM 2-mercaptoethanol (2-ME), 0.5% Triton X-100, 30 mM Imidazole and 1 mM phenylmethylsulphonyl fluoride (PMSF). LCB1 was first purified by affinity chromatography using the Ni-NTA resin (Thermo Fisher Scientific). The sample was next purified by FPLC size-exclusion chromatography using a Superdex-75 gel filtration column (Cytiva Life Sciences). Peak fractions were collected and incubated with a His-tagged TEV protease at a mass ratio of 1: 10 [TEV: 6xHis-LCB1] overnight at 4 °C for affinity tag removal. The digested protein sample was applied to Ni-NTA affinity purification and the flow-through fractions containing LCB1 without the His-tag were collected, with a molecular weight of 8.6 kDa (Figure S8, Supporting Information).

**OECT Device Fabrication:** The overall approach to device fabrication is shown schematically in Figure S3 (Supporting Information). Glass substrates were cut to dimensions of 2.54 cm × 2.54 cm and electrodes were deposited by sputtering chromium (5 nm) and gold (50 nm) sequentially through a shadow mask created using Kapton tape. The channel was then defined by etching away a portion of the electrodes using a needle, resulting in a channel width and length of 300 ± 100 and 100 ± 20  $\mu$ m, respectively. Next, a portion of the substrate was protected with Kapton tape, leaving the channel area exposed for the further fabrication process. A liquid dispersion of PEDOT:PSS with 10% (v/v) EG, 25% (v/v) PVA and 0.25% (v/v) DBSA was deposited on the channel by spin-coating at 1000 rpm for 30 s, followed by heating at 140 °C for 30 min on a hot plate to crosslink PEDOT:PSS. Last, an electrolyte well (cut from 1 mL pipette tips) was glued on top of the channel. The channel was soaked in 250  $\mu$ L PBS before functionalization.

**Device Functionalization with Protein Minibinder LCB1:** The channel was functionalized by immobilizing the protein minibinder LCB1 onto the channel surface. This was achieved by vapor depositing GOPS onto PEDOT:PSS, resulting in an epoxy-functionalized surface.<sup>[33]</sup> GOPS was deposited onto the device at 120 °C for 1 h in a closed chamber under vacuum (30 mm Hg). Next, 250  $\mu$ L of a 57  $\mu$ M solution of LCB1 in PBS buffer at pH 8.0 was added to the electrolyte well and incubated at room temperature for 4 h. The wells were then rinsed 3 times using PBS buffer (pH 7.4). 250  $\mu$ L fresh pH 7.4 PBS was added into the electrolyte wells for storage prior to testing.

**X-Ray Photoelectron Spectroscopy (XPS):** XPS analysis was performed by PHI Quantera XPS. Samples were prepared on 1 cm × 1 cm glass substrates using the same protocol as device fabrication and channel functionalization. The samples were analyzed with 50 W, 15 kV, and 200  $\mu$ m diameter X-rays, and the survey scan spectra were recorded in 0.5 eV steps with a pass energy of 140 eV in the binding energy range of 1100 to 0 eV.

**Quartz Crystal Microbalance with Dissipation Analysis (QCM-D):** QCM-D analysis was performed using Qsense E4 Quartz Crystal Microbalance. A silicon dioxide sensor was coated with a liquid dispersion of PEDOT:PSS with 10% (v/v) EG, 25% (v/v) PVA and 0.25% (v/v) DBSA by spin casting at 3000 rpm for 30 s. The sensor was heated at 140 °C for 30 min, and then GOPS was then deposited on the surface by chemical vapor deposition at 120 °C for 1 h in a vacuum oven. A control sensor without GOPS was also analyzed. For each test, PBS buffer was first injected into the chamber at a flow rate of 50  $\mu$ L min<sup>-1</sup> until the change in frequency reached a constant value. Next, LCB1 (57  $\mu$ M) was injected into the sensor chamber at a flow rate of 40  $\mu$ L min<sup>-1</sup> until the chamber was saturated. The flow was then stopped for 4 h to mimic conditions used to functionalize OECT devices, and after 4 h PBS buffer was introduced into the sample chamber at a flow rate of 50  $\mu$ L min<sup>-1</sup>. The QCM-D data is presented at the third overtone. Change in mass ( $\Delta m$ ) was calculated by using the Sauerbrey equation:  $\Delta m = -C \times \Delta f/n$ , where  $C = 17.7$  ng/(cm<sup>2</sup> Hz) is the mass sensitive constant,  $\Delta f$  is the change in frequency, and  $n$  is the overtone number.<sup>[34,35]</sup>

**OECT Characterization:** Transistor characterization was performed with a Keithley 2604B SourceMeter®, using Matlab code provided by Tektronix. Ag/AgCl was used as the gate electrode. Transfer curves which relate the source-drain current  $I_{sd}$  to the gate voltage  $V_g$  were obtained for  $V_g$  varying from -0.6 to 0.6 V with step size  $V_{step} = 0.1$  and source-drain voltage  $V_{sd} = -0.6$  V.

**Electrochemical Characterization:** Cyclic voltammetry (CV) and electrochemical impedance spectroscopy (EIS) measurements were performed using a BioLogic VMP-300 Potentiostat, with an Ag/AgCl/1 M KCl as the



reference electrode and a titanium rod counter electrode. The substrate was repatterned by using Kapton tape to cover the drain electrode, leaving the source electrode and channel to be the working electrode. For CV measurements, the applied potential ( $V_{\text{applied}}$ ) was scanned from -0.8 to +0.8 V versus Ag/AgCl/1 M KCl with a scan rate of 20 mV s<sup>-1</sup> for three cycles. For EIS measurements, a voltage of -0.6 V versus Ag/AgCl/1 M KCl was applied on the working electrode, scanned with frequencies from 100 kHz to 100 mHz and a fixed amplitude ( $V_a$ ) of 10 mV. An in-built software (EC-Lab) was used for fitting circuit analysis. The scanning window for the applied potential was changed to be  $V_{\text{applied}} = -0.3$  to +0.6 V versus Ag/AgCl/1 M KCl to evaluate surface modifications and protein attachment.

**Statistical Analysis:** Normalized response curves show average values along with standard deviations for each data points, determined by at least three independent measurements for each concentration and time. The method for determining the average and standard deviation is as follows: The normalized response (NR) is defined as the change in current  $I$  relative to the baseline  $I_0$ :  $NR = (I - I_0)/I_0$ . The baseline was first determined by measuring the source-drain current as a function of time without any protein or virus present, and the current was averaged over five devices. The current in the presence of a biomolecular target was measured as a function of time and repeated with at least three devices for each condition tested (target and concentration). The limit of detection (LOD) for each testing condition was defined as the lowest concentration that was greater than three times the noise level in the baseline (see Supporting Information for more details).<sup>[22]</sup> The LOD was calculated at 5 min time intervals for each biomolecular target. These analyses were performed in OriginLab.

## Supporting Information

Supporting Information is available from the Wiley Online Library or from the author.

## Acknowledgements

The authors acknowledge support from the Defense Advanced Research Projects Agency (DARPA, agreement no. HR00112190062 to P.J.A., Y.J.T., and R.V.), the Welch Foundation C-1565 (Y.J.T.), and the National Science Foundation (NSF) RAPID-2029339 (P.J.A. and Y.J.T.). The authors also thank Mr. Tzu-Chieh Shu and Ms. Xin-Yi Shu for designing schematics, Dr. David Baker for providing the cDNA of LCB1, and Prof. Aditya Mohite for assistance with OECT device measurements.

## Conflict of Interest

The authors declare no conflict of interest.

## Data Availability Statement

The data that support the findings of this study are available in the Supporting Information of this article.

## Keywords

biosensor, COVID-19, OECT, rapid detection, SARS-CoV-2

Received: February 2, 2023

Revised: April 25, 2023

Published online:

[1] WHO Coronavirus (COVID-19) Dashboard, (COVID-19) <https://covid19.who.int> (accessed: February 2023).

- [2] W. S. Hart, P. K. Maini, R. N. Thompson, *Elife* **2021**, *10*, e65534.
- [3] M. A. Johansson, T. M. Quandelacy, S. Kada, *JAMA Netw Open* **2021**, *4*, e2035057.
- [4] C. C. Wang, K. A. Prather, J. Sznitman, J. L. Jimenez, S. S. Lakdawala, Z. Tufekci, L. C. Marr, *Science* **2021**, *373*, eabd9149.
- [5] W. Ji, X. Li, S. Chen, L. Ren, *Proc. Natl. Acad. Sci. U.S.A.* **2021**, *118*, e2026093118.
- [6] M. Jayaweera, H. Perera, B. Gunawardana, J. Manatunge, *Environ. Res.* **2020**, *188*, 109819.
- [7] B. Udugama, P. Kadhiresan, H. N. Kozlowski, A. Malekjahani, M. Osborne, V. Y. C. Li, H. Chen, S. Mubareka, J. B. Gubbay, W. C. W. Chan, *ACS Nano* **2020**, *14*, 3822.
- [8] M. M. Hellou, A. Górska, F. Mazzaferri, E. Cremonini, E. Gentilotti, P. De Nardo, I. Poran, M. M. Leeflang, E. Tacconelli, M. Paul, *Clin. Microbiol. Infect.* **2021**, *27*, 341.
- [9] S. L. Emery, D. D. Erdman, M. D. Bowen, B. R. Newton, J. M. Winchell, R. F. Meyer, S. Tong, B. T. Cook, B. P. Holloway, K. A. McCaustland, P. A. Rota, B. Bankamp, L. E. Lowe, T. G. Ksiazek, W. J. Bellini, L. J. Anderson, *Emerg. Infect. Dis.* **2004**, *10*, 3111.
- [10] A. Roberts, R. S. Chouhan, D. Shahdeo, N. S. Shrikrishna, V. Kesarwani, M. Horvat, S. Gandhi, *Front. Immunol.* **2021**, *12*, 732756.
- [11] B. G. Andryukov, 1 *Somov Research Institute of Epidemiology and Microbiology* Vladivostok, Russian Federation, 2 Far Eastern Federal University (FEFU), Vladivostok, Russian Federation, *AIMS Microbiology* **2020**, *6*, 280.
- [12] A. Crozier, S. Rajan, I. Buchan, M. McKee, *BMJ* **2021**, n208.
- [13] J.-L. Wu, W.-P. Tseng, C.-H. Lin, T.-F. Lee, M.-Y. Chung, C.-H. Huang, S.-Y. Chen, P.-R. Hsueh, S.-C. Chen, *J. Infect.* **2020**, *81*, 435.
- [14] World Health Organization, *Antigen-Detection in the Diagnosis of SARS-CoV-2 Infection Using Rapid Immunoassays: Interim Guidance, 11 September 2020*, World Health Organization **2020**.
- [15] J. Wise, *BMJ* **2020**, m4848.
- [16] O. Calvo-Lozano, M. Sierra, M. Soler, M. C. Estévez, L. Chiscano-Camón, A. Ruiz-Sanmartin, J. C. Ruiz-Rodríguez, R. Ferrer, J. J. González-López, J. Esperalba, et al., *Anal. Chem.* **2022**, *94*, 975.
- [17] A. M. Shrivastav, U. Cvelbar, I. Abdulhalim, *Commun Biol* **2021**, *4*, 70.
- [18] T. Chaibun, J. Puenpa, T. Ngamdee, N. Boonapatcharoen, P. Athamanolap, A. P. O'Mullane, S. Vongpunsawad, Y. Poovorawan, S. Y. Lee, B. Lertanantawong, *Nat. Commun.* **2021**, *12*, 802.
- [19] N. Kumar, N. P. Shetti, S. Jagannath, T. M. Aminabhavi, *Chem. Eng. J.* **2022**, *430*, 132966.
- [20] G. Seo, G. Lee, M. J. Kim, S.-H. Baek, M. Choi, K. B. Ku, C.-S. Lee, S. Jun, D. Park, H. G. Kim, et al., *ACS Nano* **2020**, *14*, 5135.
- [21] K. Ditte, T. A. Nguyen Le, O. Ditzer, D. I. Sandoval Bojorquez, S. Chae, M. Bachmann, L. Baraban, F. Lissel, *ACS Biomater. Sci. Eng.* **2021**, <https://doi.org/10.1021/acsbomaterials.1c00727>.
- [22] K. Guo, S. Wustoni, A. Koklu, E. Díaz-Galicia, M. Moser, A. Hama, A. A. Alqahtani, A. N. Ahmad, F. S. Alhamlan, M. Shuaib, et al., *Nat. Biomed. Eng.* **2021**, *5*, 666.
- [23] J. Rivnay, S. Inal, A. Salleo, R. M. Owens, M. Berggren, G. G. Malliaras, *Nat. Rev. Mater.* **2018**, *3*, 17086.
- [24] G. L. Long, J. D. Winefordner, *Anal. Chem.* **1983**, *55*, 1432.
- [25] H. Liu, A. Yang, J. Song, N. Wang, P. Lam, Y. Li, H. K. Law, F. Yan, *Sci. Adv.* **2021**, *7*, eabg8387.
- [26] A. Chevalier, D.-A. Silva, G. J. Rocklin, D. R. Hicks, R. Vergara, P. Murapa, S. M. Bernard, L. Zhang, K.-H. Lam, G. Yao, et al., *Nature* **2017**, *550*, 74.
- [27] L. Cao, I. Goreschnik, B. Coventry, J. B. Case, L. Miller, L. Kozodoy, R. E. Chen, L. Carter, A. C. Walls, Y.-J. Park, et al., *Science* **2020**, *370*, 4267.
- [28] J. Lan, J. Ge, J. Yu, S. Shan, H. Zhou, S. Fan, Q. Zhang, X. Shi, Q. Wang, L. Zhang, et al., *Nature* **2020**, *581*, 215.

- [29] S. Inal, G. G. Malliaras, J. Rivnay, *Nat. Commun.* **2017**, *8*, 1767.
- [30] S. Klein, M. Cortese, S. L. Winter, M. Wachsmuth-Melm, C. J. Neufeldt, B. Cerikan, M. L. Stanifer, S. Boulant, R. Bartenschlager, P. Chlanda, *Nat. Commun.* **2020**, *11*, 5885.
- [31] J. R. Thompson, Y. V. Nanchaiah, X. Gu, W. L. Lee, V. B. Rajal, M. B. Haines, R. Girones, L. C. Ng, E. J. Alm, S. Wuertz, *Water Res.* **2020**, *184*, 116181.
- [32] A. Bivins, D. North, A. Ahmad, W. Ahmed, E. Alm, F. Been, P. Bhattacharya, L. Bijlsma, A. B. Boehm, J. Brown, et al., *Environ. Sci. Technol.* **2020**, *54*, 7754.
- [33] J. T. Borges, L. Y. K. Nakada, M. G. Maniero, J. R. Guimarães, *Environ. Sci. Pollut. Res.* **2021**, *28*, 40460.
- [34] J. R. Sempionatto, J. A. Lasalde-Ramírez, K. Mahato, J. Wang, W. Gao, *Nat Rev Chem* **2022**, *6*, 899.
- [35] J. Y. Oh, S. Rondeau-Gagné, Y.-C. Chiu, A. Chortos, F. Lissel, G.-J. N. Wang, B. C. Schroeder, T. Kurosawa, J. Lopez, T. Katsumata, et al., *Nature* **2016**, 539, 411.
- [36] Y. Zheng, Z. Yu, S. Zhang, X. Kong, W. Michaels, W. Wang, G. Chen, D. Liu, J.-C. Lai, N. Prine, et al., *Nat. Commun.* **2021**, *12*, 5701.
- [37] S. Bontapalle, M. Na, H. Park, K. Sim, *Chem. Commun.* **2022**, *58*, 1298.
- [38] J. Chen, W. Huang, D. Zheng, Z. Xie, X. Zhuang, D. Zhao, Y. Chen, N. Su, H. Chen, R. M. Pankow, et al., *Nat. Mater.* **2022**, *21*, 564.
- [39] M. Zabhipour, R. Lassnig, J. Strandberg, M. Berggren, S. Fabiano, I. Engquist, P. Andersson Ersman, *Npj Flex Electron* **2020**, *4*, 15.
- [40] W. Wang, Z. Li, M. Li, L. Fang, F. Chen, S. Han, L. Lan, J. Chen, Q. Chen, H. Wang, et al., *Nano-Micro Lett.* **2022**, *14*, 184.
- [41] D. Liu, X. Tian, J. Bai, Y. Wang, Y. Cheng, W. Ning, P. K. L. Chan, K. Wu, J. Sun, S. Zhang, *Adv. Sci.* **2022**, *9*, 2203418.